

Incorporating Polarization in Stereo Vision-based 3-D Perception of Non-Lambertian Scenes

Kai Berger^a, Randolph Voorhies^b and Larry Matthies^a

^aJet Propulsion Laboratory, Pasadena, CA, USA

^binVia Robotics, Agoura, CA, USA

ABSTRACT

Surfaces with specular, non-Lambertian reflectance are common in urban areas. Robot perception systems for applications in urban environments need to function effectively in the presence of such materials; however, both passive and active 3-D perception systems have difficulties with them. In this paper, we develop an approach using a stereo pair of polarization cameras to improve passive 3-D perception of specular surfaces. We use a commercial stereo camera pair with rotatable polarization filters in front of each lens to capture images with multiple orientations of the polarization filter. From these images, we estimate the degree of linear polarization (DOLP) and the angle of polarization (AOP) at each pixel in at least one camera. The AOP constrains the corresponding surface normal in the scene to lie in the plane of the observed angle of polarization. We embody this constraint an energy functional for a regularization-based stereo vision algorithm. This paper describes the theory of polarization needed for this approach, describes the new stereo vision algorithm, and presents results on synthetic and real images to evaluate performance.

Keywords: stereo vision, non-Lambertian, polarization, 3D perception

1. INTRODUCTION

Robot perception systems for autonomous mobility and manipulation depend heavily on 3-D perception. Most 3-D perception systems explicitly or implicitly assume scenes with Lambertian reflectance, and often perform poorly for materials that are significantly non-Lambertian, such as specular and transparent surfaces. 3-D perception of specular scenes has been addressed in various ways in the past, including with multi-baseline stereo, known active illumination, and other methods, but to our knowledge, no perception system exists today

Further author information: (Send correspondence to Kai Begrer)

E-mail: kuberger@jpl.nasa.gov

Copyright 2016. All rights reserved.

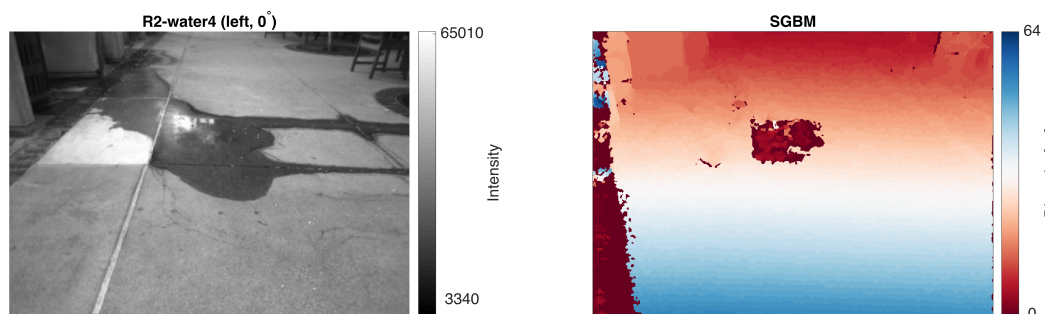


Figure 1. Specular surfaces (water puddle, left) usually pose a challenge to state-of-the-art stereo vision algorithms (right, an example result using the SGBM algorithm¹): In this case parts of the patio are reconstructed as being further from the camera than they really are.

that understands this phenomenology in a deep way and provides high quality 3-D perception for general robotics applications for common specular materials.

Many environments have unpolarized illumination and specular surfaces that linearly polarize reflected light. In these cases, polarization cameras can provide information to improve 3-D perception. By acquiring images with a linear polarization filter at multiple orientations, the degree of linear polarization (DOLP) and the angle of polarization (AOP) can be estimated at each pixel in the image. The AOP is coplanar with the corresponding surface normal in the scene, so it can be taken as a constraint on the surface normal. The DOLP indicates which pixels are sufficiently polarized that the AOP may be useful.

In this paper, we incorporate such polarization-based measurements into a novel stereo vision algorithm to improve passive 3-D perception of specular surfaces. We do not explicitly address the possibility that the surface is also transparent, so we effectively assume that surfaces are opaque. Stereo vision algorithms have often been formulated as energy minimization problems, with assumptions about the presence of smooth surfaces in the scene embodied as penalty terms on surface gradients or curvatures in the energy functional. We extend such a formulation to include the surface normal constraints from polarization. We use an existing graph cuts-based optimization algorithm to compute a stereo disparity map that approximately minimizes the energy functional. We test this approach with synthetic images with perfect ground truth and with real images acquired with a stereo camera pair with arbitrarily rotatable linear polarizers fixed in front of each lens. We use scenes from urban environments, including indoor (like in a hallway) and outdoor (like a patio) scenarios (Fig 1).

Section 2 discusses prior work and the shortcomings of conventional depth from stereo for non-Lambertian scenes in more detail. We describe how to generate simulated stereo imagery with a polarization-aware backward tracing algorithm based on the Jones Calculus in section 3. Using the simulator, we have perfectly rectified stereo images and ground truth disparities for quantitative performance evaluation. We acquire real-world imagery with our stereo-polarization camera setup and provide pseudo-ground truth for these scenes by having a user click corresponding points in the images to designate known planar surfaces (section 4). We describe our 3-D reconstruction algorithm and compare it to an existing approach that is very popular in autonomous system applications in section 5. Section 6 draws conclusions.

2. RELATED WORK

First approaches to handle specularities in stereo vision mainly focused on specular highlights on reflective surfaces.^{2,3} The introduction of a third camera in a trinocular setup was used to improve results in this case by picking pairs of images that were not affected by small specularities.⁴ Extensions to multi-camera approaches followed;⁵⁻⁷ however, most of this work focused on specular highlights and did not address the superposition of reflections and diffusely reflected patterns over large surface areas. This problem was addressed explicitly by Tsin et al⁸ for static, indoor environments with a plane sweep-based algorithm that attempted to reconstruct surfaces and their intrinsic surface patterns. This work is interesting, but the number views necessary to achieve the results was not discussed, nor was the computational complexity of the algorithm; it remains to be seen how well this approach applies in other settings.

Time of flight laser rangefinders can estimate range to shiny materials that also have a diffuse component of reflection; however, this capability degrades with increasing specularity and increasing angle of incidence of the beam on the surface.⁹ For shiny surfaces that also have a diffuse component of reflection, methods based on structured light can be employed;¹⁰⁻¹³ however, these are limited to fairly short range by limitations on the optical power of the structured light emitter, eye safety, and where there is strong ambient illumination (e.g. outdoors).

Taking the temporal aspect in account, it is possible to decompose the optical flow in between multiple frames of a monocular image sequence into multiple layers, such as a diffuse and a specular flow. Given knowledge of camera motion, it is possible to reconstruct the shape of shiny objects this way;¹⁴ however, work to date in this direction has assumed simple illumination with a distant light source, twice-differentiable surfaces, and has only been tested on simple scene geometries. Nevertheless, this may be an interesting approach to combine with the methods used here in the future.

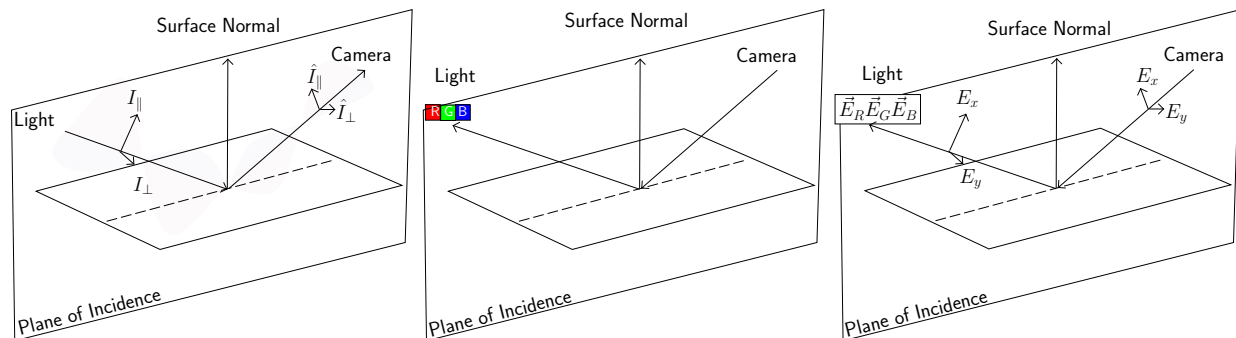


Figure 2. Modeling the polarization phenomenology of reflective surfaces (left) in nature: We implement a backward tracing approach²³ for the generation of our virtual scenes. While a standard ray tracer stores a triplet of real numbers for each pixel being traced (middle), we store a triplet of Jones vectors to account for the polarization behavior of the light (right).

Polarization has been used for several computer vision applications, such as material classification and separating the specular and diffuse component of a reflection.^{15,16} The angle of polarization (AOP) in an image constrains the corresponding 3D surface normal to line in a plane defined by the AOP vector and the center of projection. With additional information about the index of refraction of the material, the full surface normal can be recovered;¹⁵ however, in our applications, the index of refraction is unknown. Shape-from-shading-like algorithms can be used to reconstruct the scene up to an unknown scale factor using such measurements.^{17–19} Polarization information from defined point light sources have been employed in an approach²⁰ to reconstruct the shape of smooth specular objects. Also, an approach has been presented to combine Kinect depth data with polarization information from an additional camera,^{13,21} but the reconstruction is limited by the maximum depth returned from the Kinect.

Using the AOP as a surface normal constraint in a stereo algorithm was proposed by Wolf,¹⁵ but he did not develop an algorithm to do so. We adapt an approach based on graph cuts²² and augment the energy function such that it combines a robust data term, a second-order surface smoothness prior, and a polarization-based the constraint on the surface normal, which is derived from the measured AOP at each pixel. Both the surface normal constraint and the second-order smoothness prior lead to ternary terms in the energy function and a difficult optimization problem. Similar to Woodford,²² we formulate these as combinations of binary terms, and we employ their estimation algorithm, which is based on quadratic pseudo-boolean optimization, to arrive at a close-to-optimal depth map. Tests with simulated stereo polarization imagery of an indoor scene and various real scenes acquired indoors and outdoors show that our approach results in better depth maps than leading stereo algorithms for autonomous system applications that do not incorporate the polarization information.

3. GENERATING VIRTUAL SCENES

Algorithm development and initial validation is far easier with synthetic imagery with known polarization properties and exact ground truth for stereo disparities than with real images of complex scenes, for which it is hard to obtain ground truth. Therefore, we have extended a ray tracing-based scene rendering package to model polarization in order to have such synthetic test imagery.

3.1 Mathematical Background

First we have to represent the polarized light transport with a suitable mathematical framework. We chose the Jones calculus for that. In this framework the polarization state of a light wave is described by vector $\vec{E} = (E_x, E_y)^\top$ consisting of two complex numbers, Fig. 2 (right). Some examples of this vector are the linearly polarized light waves at angles $0^\circ, 45^\circ, 90^\circ$, and 135° : $\vec{E}_{0^\circ} = (1, 0)$, $\vec{E}_{90^\circ} = (0, 1)$, $\vec{E}_{45^\circ} = (1, 1) \cdot \frac{1}{\sqrt{2}}$, and $\vec{E}_{-45^\circ} = \vec{E}_{135^\circ} = (1, -1) \cdot \frac{1}{\sqrt{2}}$. A linear polarizer can be expressed by the identity matrix, where the second diagonal element is set to zero. Rotating that polarizer to any angle with respect to a global up-vector is performed by multiplying the matrix with a 2D rotation matrix accordingly. To incorporate Fresnel-governed

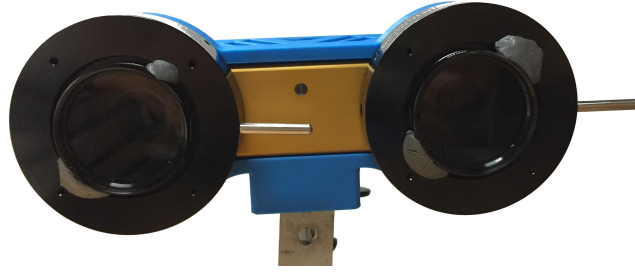


Figure 3. We capture real-world scenes with a Bumblebee 2 stereo camera system with an external fixture comprising two rotatable linear polarizers. The rotations can be set arbitrarily.

reflection behavior into the Jones calculus, we compute the parallel and perpendicular reflection from the Fresnel equations and set the diagonal elements of a complex 2D matrix accordingly.

3.2 Implementation of Backward Tracing for Polarized Reflection

We implement a backward tracing approach,²³ Fig. 2 (middle), with the exception that we use a Jones-Vector (two complex numbers) for each color represented in a ray, Fig 2 (right). Since Jones Calculus can only be applied to light waves that are partially or fully polarized, we perform the following procedure to generate images that also contain purely Lambertian surfaces. First, we set the Jones matrices for all Lambertian surfaces to the identity matrix, and we set the Jones vectors emitted by the light sources to $\vec{E} = (a, a * \mathbf{i})$, $a \in \mathcal{R}$ and save the result of the backward tracing²³ as I_d . Afterwards, we trace the light transport for reflective surfaces that have an effect on the polarization behavior of the light by assigning the Fresnel-governed reflection behavior to the shaders for these surfaces. We may look up results from the first ray tracing round if a backwardly traced ray from a reflective surface hits a purely Lambertian surface. We store the result in $I_s \in \mathcal{C}^3$. The final image is generated by combining $I_{final} = I_d + I_s \in \mathcal{C}^3$

3.3 Viewing Toolkit

We implement a viewing toolkit in MATLAB that combines both I_d and I_s while allowing the user to specify the rotation of a virtual linear polarizer which is placed in front of the camera. This way, the viewer can experience the polarization effects present in the scene, by varying the rotation angle of the virtual linear polarizer. The toolkit computes the matrix multiplication of the matrix for the virtual linear polarizer with the Jones vectors at each pixel stored in I_s on the fly. The displayed intensity is retrieved by computing the Euclidean norm of the resulting Jones vector.

3.4 Ground Truth: Depth, Normals, Stereo

The the backward tracing algorithm is initialized with two camera positions, C_1 and $C_2 = C_1 + b$, where b denotes the baseline offset, which is perpendicular to the viewing axis of C_1 and C_2 ; i.e. we assume both viewing axes to be parallel to each other. After evaluating the light transport in the scene, another backward tracing iteration is performed, but the recursive ray tracing essential to reflective surfaces is disabled this time. First the depth image D is computed by taking the hit position of the ray with a surface in the scene and evaluating its distance to the image plane with $\frac{\text{Dot}(\vec{x}_{hit} - (\vec{x}_{cam} + \vec{view} \cdot \text{focus}), \vec{view})}{\text{Dot}(\vec{view}, \vec{view})}$. The normal image N is computed by passing the the surface normal \vec{x}_{hit} of each surface in the scene hit by a ray and assigning it to a color value. Note that the normals range is in $[-1..1]$. The disparity image is computed by tracing a ray from a pixel position (x, y) in the left image into the scene and then by back projecting the hit position into the right camera with $(\frac{\text{Dot}(\vec{x}_{hit} - (\vec{x}_{cam} + \vec{view} \cdot \text{focus}), x\vec{Axis})}{\text{Dot}(x\vec{Axis}, x\vec{Axis} \cdot D)} \cdot x\text{Resolution}) - x$ and subtracting it from the left image's pixel position.

4. ACQUIRING REAL IMAGERY

Real-world images used here were acquired with a PointGrey Bumblebee BB2-08s2C stereo camera pair equipped with an external fixture that places linear polarizers in front of each lens, Fig. 3. Both polarizers can be rotated

arbitrarily, but for our purposes we use the rotations $0^\circ, 45^\circ, 90^\circ, 135^\circ$. We acquire the images sequentially for each polarization angle using Matlab's Image Acquisition toolbox, which requires the scene to remain still in between the four frame captures. We have more recently acquired polarization cameras that use micro-grid polarization filters on the focal plane to acquire four polarization channels simultaneously; result with these cameras will be reported in the future.

5. ALGORITHM DESCRIPTION AND PERFORMANCE EVALUATION

This section describes how we incorporate polarization into our stereo vision algorithm and compares its performance to one of the currently most popular stereo vision algorithms for autonomous system applications, the semi-global block matching algorithm (SGBM).²⁴ We begin with a short summary of SGBM, then describe our algorithm, data sets used for performance evaluation, and the performance comparison between these two approaches.

5.1 SGBM

SGBM uses multi-directional dynamic programming to find a disparity map that minimizes a cost function that measures the similarity of corresponding pixels and deviations from zero disparity gradient over the whole image. The optimum depth map is found minimizing the following cost function:²⁴

$$E(D) = \sum_p C(p, D_p) + \sum_{q \in N_p} P_1 T[|D_p - D_q| = 1] + \sum_{q \in N_p} P_2 T[|D_p - D_q| > 1] , \quad (1)$$

where D is the estimated disparity map. The first term is a photo-consistency term, summed over all pixels p , that uses a cost function C to measure the similarity of corresponding pixels given the disparity $D(p)$. The second summation penalizes small disparity changes between pixel p and pixels q in the neighborhood of p ; the third summation penalizes large disparity changes.

5.2 Graph-Cut with Surface Normal Constraint

We base our energy functional definition on the one described by Woodford et al.:²²

$$E_{\text{photo+smoothness}} = \sum_x f(\Pi(x, D(x)) - I_0(x), V) + \sum_{\mathcal{N} \in N} W(\mathcal{N}) \rho(\mathcal{S}(\mathcal{N}, \mathcal{D})) \quad (2)$$

The first summation again is a photo-consistency term, where f is a robust photo-consistency metric, $D(x)$ is the disparity at pixel x , Π the projection matrix between the two cameras, I_0 the image of the left camera, and V is a visibility flag indicating whether a given pixel is occluded. The second term penalizes departures from smoothness in the disparity map, where \mathcal{S} is a disparity derivative computed over 3×1 and 1×3 pixel horizontal and vertical neighborhoods \mathcal{N} , ρ is a truncated absolute value applied to \mathcal{S} , \mathcal{D} is the disparity map, and W is a weight that relaxes the smoothness penalty around intensity edges in the image. We augment the energy functional as follows:

$$E_{\text{photo+smoothness}} = \sum_x f(\Pi(x, D(x)) - I_0(x), V) + \sum_{\mathcal{N} \in N} W_1(\mathcal{N}) \rho(\mathcal{S}(\mathcal{N}, \mathcal{D})) + \sum_x W_2(\mathcal{N}(x)) \rho(\mathcal{A}(\mathcal{N}(x), \mathcal{D}, \theta(x))) \quad (3)$$

with $\theta(x)$ the angle of polarization at a given pixel x , $\mathcal{N}(x)$ the clique containing pixel x and \mathcal{A} defined as

$$\mathcal{A}(\{p, q, r\}, \mathcal{D}, \theta) = \tan^{-1}(\Gamma((\Pi^{-1}(p, D(p)) - \Pi^{-1}(q, D(q)) \times \Pi^{-1}(r, D(r)) - \Pi^{-1}(q, D(q)))) - \theta), \quad \{p, q, r\} \in \mathcal{N} \quad (4)$$

where $\{p, q, r\}$ are consecutive pixels in the 3×1 and 1×3 neighborhoods described above. The function $\Gamma(\cdot)$ back projects the surface normal into the image plane. this term creates a local surface normal by back projecting the three nodes and then retrieves the angle between the normal and the global up-vector. The difference from

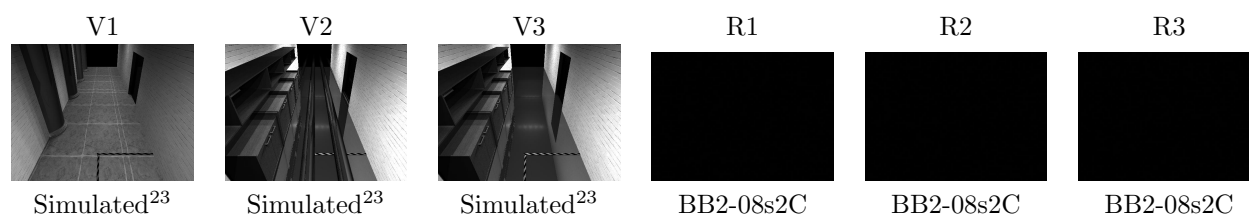


Table 1. We compare our approach to the SBGM algorithms on the depicted virtual (v1-3) and real-world (r1-3) scenes. See section 5.3 for more description.

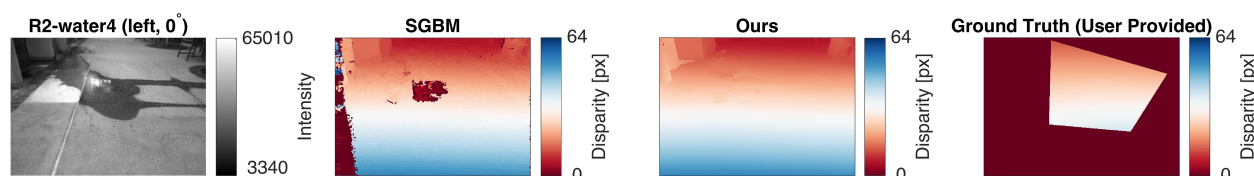


Figure 4. Applying our algorithm to the water scene results in a disparity map that is closer to the ground truth than SGBM. We provide the ground truth by finding a planar homography between corresponding image points that are designated by a user.

the resulting angle and the captured angle of polarization from the left camera is then sought to be minimized. Recall, that first-order priors tend to bias depth reconstructions to fronto-parallel surfaces.

With the energy function defined, a critical question is how to find a disparity map that minimizes it. This function is not submodular, so no methods are available to find a global optimum. We follow Woodford et al.²² by modifying their software for quadratic pseudo-boolean optimization to use our energy function. This technique searches iteratively for better minima given an initial estimate. After experimentation with various approaches to making initial estimates, we opted to use the degree of partial linear polarization estimated at each pixel to classify pixels as either diffuse or specular. We use SGBM to compute an initial disparity map for the diffuse pixels. Our energy function is then used to find estimates for the specular pixels. As such, the method currently uses the smoothness prior and polarization-based surface normal constraints to interpolate and extrapolate the disparity of specular pixels. We discuss this issue again below.

5.3 Data for Evaluation

We evaluate the approaches with three virtual scenes generated with the polarization-aware backward tracing approach and with three real-world scenes, see Table 1. Simulated scene V1 is a hallway with diffuse surfaces and two shiny columns on the left wall to test performance of our method on curved surfaces. Simulated scenes V2 and V3 are hallways created to mimic real scene R1. All of these scenes have a shiny floor with reflections superimposed on intrinsic albedo patterns in the floor. In V2 we have also included half-cylinder “pipes” on the floor as another test of performance on curved surfaces, where here the surface normal discontinuity is oriented quite differently than in V1. Real scene R2 is the patio with a puddle, shown in Fig 1. Real scene R3 is a diffuse exterior building wall with a glass door.

5.4 Performance Comparison

Fig. 4 compares disparity maps produced by SGBM and our algorithm for the patio scene with a water puddle (R2). In this case, polarization finds the wet areas and the end. Further, we show the results of SGBM and Our approach on all scenes in Fig. 5 as histograms of the L_1 distance of the generated disparity map to the ground truth disparity map. The closer all L_1 distances to zero, the more accurately the produced disparity map approximates the ground truth scene disparity.

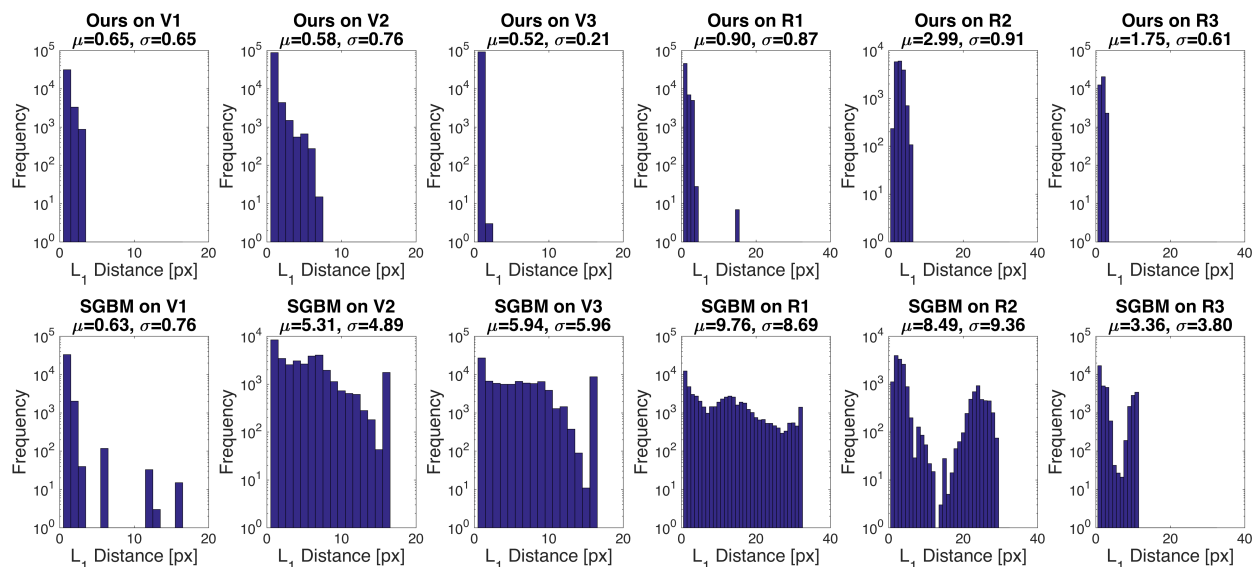


Figure 5. We compute the L_1 distance (in px) for the resulting disparity maps of Our approach and SGBM to the ground truth disparity maps and bin the frequency of each occurring distance. Further, we compute the average L_1 distance and the standard deviation from the average distance. Note that the frequencies are displayed on logarithmic scale for visibility.

It can be seen that SGBM is challenged by the specularities. In scene V2, the result of SGBM compares well to our result. However, this is due to the pipe-floor edge which provides an important cue for assigning a close-to-correct disparity. For the real-world scene R1, the hallway floor, which is a PVC material, is too shiny to contribute to a meaningful disparity reconstruction and SGBM produces disparity values in the pixel region comprised by the floor that are greater than they should be, corresponding to the virtual disparity of the reflection. Our approach performs well on scenes V1, V2 and V3 and approach overcomes the effects introduced by the specular materials in the real-world scenes R1-R3, such that the disparities of the corresponding surfaces are approximated correctly.

6. CONCLUSION

We presented an approach to 3-D perception of specular scenes. While this has been addressed previously with a variety of approaches, prior methods do not fully solve the problem of giving absolute range in unstructured settings. Our approach is the first to incorporate polarization behavior of the reflected light in a stereo vision algorithm, which we do by using the measured degree and angle of linear polarization at each pixel in the image to constrain the surface normal at each pixel that shows an appreciable degree of polarization. We formulated an energy function that combines terms for photoconsistency, a second-order surface smoothness prior, and the polarization-based surface normal constraint. A near-optimal disparity map estimate is found via quadratic pseudo-boolean optimization. Experimental results with synthetic and real images show significant improvement over the very commonly-used semi-global block matching algorithm. The real image data sets presented here were acquired with manually rotated polarization filters on each camera; work now in progress is using cameras with focal planes that simultaneously acquire images with four orientations of linear polarization. The current implementation is quite slow; future work will address runtime and extensions to more general, indoor/outdoor cases of non-Lambertian reflectance.

REFERENCES

- [1] Hirschmüller, H., “Stereo processing by semiglobal matching and mutual information,” *Transactions on Pattern Analysis and Machine Intelligence* **30**(2), 328–341 (2008).

- [2] Blake, A., "Specular stereo," in [*International Joint Conference on Artificial Intelligence*], (1985).
- [3] Blake, A. and Brelstaff, G., "Specular stereo," in [*International Conference on Computer Vision*], (1988).
- [4] Bhat, D. N. and Nayar, S. K., "Stereo and specular reflection," *International Journal of Computer Vision* **26**(2), 91–106 (1998).
- [5] Jin, H., Yezzi, A. J., and Soatto, S., "Variational multiframe stereo in the presence of specular reflections," in [*International Symposium on 3D Data Processing, Visualization, and Transmission*], (2002).
- [6] Bonfort, T. and Sturm, P., "Voxel carving for specular surfaces," in [*International Conference on Computer Vision*], (2003).
- [7] Yang, R., Pollefeys, M., and Welch, G., "Dealing with textureless regions and specular highlights: a progressive space carving scheme using a novel photo-consistency measure," in [*International Conference on Computer Vision*], (2003).
- [8] Tsin, Y., Kang, S. B., and Szeliski, R., "Stereo matching with linear superposition of layers," *IEEE Transactions on Pattern Analysis and Machine Intelligence* **28**(2), 290–300 (2006).
- [9] Hebert, M. and Krotkov, E., "3D measurements from image laser radars: how good are they?," *International Journal of Image and Vision Computing* **10**(3), 170–178 (1992).
- [10] Magda, S., Zickler, T., Kriegman, D. J., and Belhumeur, P. N., "Beyond Lambert: reconstructing surfaces with arbitrary BRDFs," in [*International Conference on Computer Vision*], (2001).
- [11] Mallick, S. P., Zickler, T., Kriegman, D. J., and Belhumeur, P. N., "Beyond Lambert: reconstructing specular surfaces using color," in [*Conference on Computer Vision and Pattern Recognition*], (2005).
- [12] Lamond, B., Peers, P., Ghosh, A., and Debevec, P., "Image-based separation of diffuse and specular reflections using environmental structure illumination," in [*International Conference on Computational Photography*], (2009).
- [13] de La Garanderie, G. P. and Breckon, T., "Improved depth recovery in consumer depth cameras via disparity space fusion within cross-spectral stereo," in [*British Machine Vision Conference*], 417–1 (2014).
- [14] Roth, S. and Black, M. J., "Specular flow and the recovery of surface structure," in [*Conference on Computer Vision and Pattern Recognition*], (2006).
- [15] Wolff, L. B. and Boulton, T. E., "Constraining object features using a polarization reflectance model," *Transactions on Pattern Analysis and Machine Intelligence* **13**(7), 635–657 (1991).
- [16] Nayar, S. K., Fang, X.-S., and Boulton, T. E., "Separation of reflection components using color and polarization," *International Journal of Computer Vision* **21**(3), 163–186 (1997).
- [17] Atkinson, G., Hancock, E. R., et al., "Recovery of surface orientation from diffuse polarization," *Transactions on Image Processing* **15**(6), 1653–1664 (2006).
- [18] Herrera, S. E. M., Malti, A., Morel, O., and Bartoli, A., "Shape-from-polarization in laparoscopy," in [*International Symposium on Biomedical Imaging*], 1412–1415, IEEE (2013).
- [19] Photon-X. www.photon-x.com/.
- [20] Ngo Thanh, T., Nagahara, H., and Taniguchi, R.-i., "Shape and light directions from shading and polarization," in [*Conference on Computer Vision and Pattern Recognition*], 2310–2318 (2015).
- [21] Kadambi, A., Taamazyan, V., Shi, B., and Raskar, R., "Polarized 3d: High-quality depth sensing with polarization cues," in [*International Conference on Computer Vision*], 3370–3378 (2015).
- [22] Woodford, O., Torr, P., Reid, I., and Fitzgibbon, A., "Global stereo reconstruction under second-order smoothness priors," *Transactions on Pattern Analysis and Machine Intelligence* **31**(12), 2115–2128 (2009).
- [23] Whitted, T., "An improved illumination model for shaded display," in [*SIGGRAPH*], **13**(2), 14, ACM (1979).
- [24] Hirschmüller, H., "Accurate and efficient stereo processing by semi-global matching and mutual information," in [*Computer Society Conference on Computer Vision and Pattern Recognition, 2005*], **2**, 807–814, IEEE (2005).